This paper appears in IEEE Transactions on Haptics, 2020.
DOI: 10.1109/TOH.2020.2988495

Dynamic Reconfiguration of Redundant Haptic Interfaces for Rendering Soft and Hard Contacts

Ali Torabi, Kourosh Zareinia, Garnette Roy Sutherland, Mahdi Tavakoli

***Abstract*—There are conflicting objectives between required characteristics of haptic interfaces such as maximum force feedback capability versus back-drive friction, which can be optimally traded-off in a redundant haptic interface; a redundant haptic interface has more degrees of freedom than minimally required ones for a given task. In this paper, a contact-aware null-space control approach for redundant haptic interfaces is proposed to address these trade-offs. First, we introduce a task-dependent null-space controller in which the internal motion of the redundant haptic interface is appropriately controlled to achieve a desired performance; i.e., low back-drive friction in case of free-space motion and soft contact or large force feedback capability in case of stiff contact. Next, a transition method is developed to facilitate the adaptation of the null-space controller's varying objectives according to the varying nature of the task. The transition method prevents discontinuities in the null-space control signal. This transition method is informed by a proposed actuator saturation observer that monitors the distance of joint torques from their saturation levels. The overall outcome is an ability to recreate the feelings of soft contacts and hard contacts with higher fidelity compared to what a conventional non-redundant haptic interface can achieve. Simulations are provided throughout the paper to illustrate the concepts. Moreover, experimental results are reported to verify the effectiveness of the proposed control strategies. It is shown that the proposed controller can perform well in the soft-contact, hard-contact, and transition phases.**

***Index Terms*—Haptics; User Interfaces; Kinematics Redundancy.**

I. Introduction

High-fidelity haptic feedback, which is critical to the safety and success of any interaction, requires appropriate haptic interface (HI) design and control [1]. The HI's workspace, maneuverability, degrees of freedom, and sensory feedback should ideally match the intuitive movements of the user's hand to induce the experience and sensation of direct touch [2]. There are several commercially available HIs, each of which has its advantages and disadvantages [3]–[5]. This, in part, relates to unavoidable trade-offs in the design specifications for a specific application. HI should simultaneously satisfy requirements of low inertia and back-drivability for ease of movement and excellent control as well as the capability of providing large enough stiffness and forces to cover reflected forces from stiff contacts. Also, the Z-width of the HI, which represents the range of impedances that it can stably display to the user, needs to be large enough to present rich haptic information to the user. A small Z-width can make it hard to distinguish between different environments because they are presented as similar impedances [6]. In addition to the above requirements, an HI needs to have a practical workspace that will allow efficient and smooth navigation of the environment, while having a small enough footprint for mobility and ease of integration in the user's workstation. Due to these reasons, the design and optimization of haptic robots have been widely studied [7], [8].

A possible approach to address the above-mentioned design trade-offs is employing kinematic redundancies in the HI design. A kinematically redundant manipulator has more degrees of freedom (DoF) than required to implement a task. Redundancy in the joint-space of a manipulator enables possible joint motions that do not change the position and orientation of the end-effector. This inner joint motion is commonly referred to as self-motion. The self-motion of a redundant manipulator can be used to achieve a secondary objective while performing a primary task [9]. The secondary objectives involve, e.g., singularity avoidance, manipulability enhancement, or force feedback capability maximization of the robot while the primary tasks involve, e.g., position, force, or impedance control of the robot in the Cartesian space. The human users commonly employ the same approach; using kinematic redundancies of their arm to perform complex dexterous tasks or stabilize hand movements while performing a primary task. In [10], it is shown that experienced surgeons exploit their arm redundancies more than the novice surgeons.

Redundant manipulators have been widely used in industrial applications [11]. Recently, it has been shown that the self-motion capability of a redundant manipulator is very promising in control of physical human-robot interactions as it can be employed to improve the overall performance of the interaction while performing a primary task [12]. Despite the promising features of RHIs, only limited attention has been paid to their design and control. The rest of the literature mostly concerns redundant robot arms for object manipulation or physical human-robot interactions with industrial robots. Industrial robots are either mechanically designed for fast motion at the end-effector or large payload capability. On the other hand, the HI's design needs to address these two conflicting requirements at the same time in addition to being

* This research was supported in part by the Canada Foundation for Innovation under Grant LOF 28241, in part by the Alberta Innovation and Advanced Education Ministry through Small Equipment under Grant RCP-12-021, in part by the Natural Science and Engineering Research Council of Canada through the Collaborative Health Research Projects, and in part by the Quanser, Inc.

A. Torabi and M. Tavakoli are with the Department of Electrical and Computer Engineering, University of Alberta, Edmonton, AB, Canada. {ali.torabi, mahdi.tavakoli}@ualberta.ca

K. Zareinia is with the Department of Mechanical Engineering, Ryerson University, Toronto, Canada. kourosh.zareinia@ryerson.ca

G. Sutherland is with the Project neuroArm, Faculty of Medicine, University of Calgary, Calgary, AB, Canada. garnette@ucalgary.ca

back-drivable and having low apparent inertia and low friction. This imposes additional design constraints and makes the design and control of HIs different from industrial robots.

In the literature, there are few studies on the design of RHIs. One of the papers on the design of an RHI is [13], but the design does not meet several of the design criteria of HIs as the designed RHI is not back-drivable and has large apparent inertia. Baser *et al.*also designed a 7-DoF RHI with a relatively larger workspace in compare to 6-DoF non-redundant HIs without enlarging the RHI's links length [14], [15]. The da Vinci Surgical System (Intuitive, Inc. CA, USA) has an RHI but no design-related information is available for proprietary reasons [16]. In [17], it is shown that the apparent inertia and manipulability of an RHI are respectively upper bounded and lower bounded to those of a non-redundant HI (NHI) that is formed by the distal set of DoFs that span the operational space. In other words, if additional DoFs are added to the base of an NHI, the apparent inertia and manipulability of the resulting RHI are only better than those of the NHI. Barrow *et al.* [18], Kim *et al.* [19], and Gosselin *et al.* [20] added one degree of redundancy to the base of HIs to enlarge their workspaces, however, there is no discussion about the redundancy resolution in these papers. Nath *et al.* [21] studied the teleoperation of a redundant manipulator using an RHI of the same number of DOFs. The rest of the literature has focused on redundant slave robots, e.g., for teleoperation. In [22], a controller is developed for a redundant slave robot for manipulability enhancement in a teleoperation system with time-varying delays. In [23], the performance of a teleoperated system with a redundant slave robot is studied.

There is also another category of redundancy for the haptic interfaces that is actuation redundancy [24]–[26]. This type of redundancy is only possible for the parallel robot [27]. The main advantage of serial robots over parallel robots is their relatively larger workspace. Also, the forward kinematics problem for serial robots has a closed-form mathematical solution. For the parallel robot, usually, this is not the case and the forward kinematics problem needs to be solved numerically, which is very computationally expensive. Parallel robots have relatively larger force feedback capability than serial robots. Also, actuation redundancy can be incorporated to render an environment with very high stiffness. The drawback of actuation redundancy for parallel robots is that having actuators instead of passive joints makes the apparent inertia and reflected friction at the end-effector of the robot larger, which is not desirable for the free-space movement.

A serial RHI can be considered as the addition of one or more extra DoFs to the base of an NHI (see Fig. 1). Compared to this NHI, the RHI has several intrinsic advantages. For instance, the RHI has smaller apparent inertia in any arbitrary direction than that of the NHI in the same direction. As shown in [28], when an HI cannot provide enough static force feedback to render an environment with high stiffness, the stiff contact feeling can be reproduced by using acceleration feedback. Having small apparent inertia for the HI helps to provide a broad range of stiffnesses [29], making the use of RHIs advantageous. Another intrinsic advantage of the RHI over the NHI is its larger effective manipulability. This means

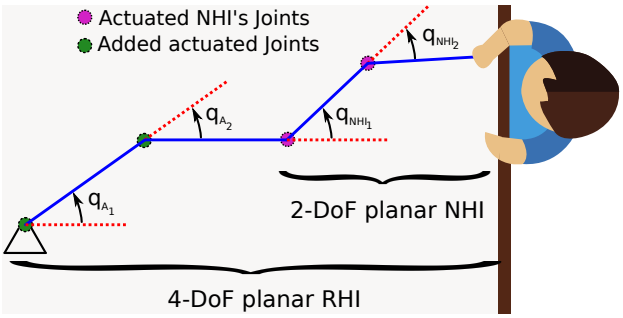

Fig. 1. Schematics of a planar RHI.

that the user requires to move the joints of the RHI less than the joints of the NHI for the same Cartesian space movement, exciting less joint friction [17]. Therefore, the RHI can display forces to the user with higher fidelity than the NHI.

In this paper, two contradictory secondary objectives are introduced for soft contacts and hard contacts. In free-space movement and soft-tissue manipulation, the RHI should have low friction and low apparent inertia so that the kinematics and dynamics of the RHI do not interfere with the user-environment interaction. In the hard-contact case, however, the RHI should have large force feedback capability and stiffness so that it can recreate the feeling of contact with solid objects. For instance, for neurosurgery applications, the RHI should satisfy the requirements of low back-drive friction and inertia so that its mechanical properties do not conceal the small interaction forces involved in the soft-tissue manipulation. Also, the RHI requires to provide large force feedback such that hard contacts with bones can be rendered for the user with a high degree of fidelity [30]. As another example, in physical rehabilitation environments for people with disabilities such as stroke, an impaired user performs repetitive free-space tasks (e.g., reaching movements). Sometimes, a human therapist or a computer algorithm needs to apply large forces to the user's hand to either assist the user in performing a task or resist the user's movements to build their muscle strength, or provide body weight support. In the free-space movement case, the back-drive friction of the RHI must be minimized in order to not fatigue the physically weak patient or impede their motion. In the assistive and resistive therapy case, the RHI needs to reflect large forces to the user similar to what is needed during hard contacts [31], [32].

As the requirements of the task varies with respect to time (switching from soft contact to hard contact), one or more of the RHI actuators may saturate. Therefore, in this paper, an actuator saturation controller is proposed based on an actuator saturation observer. The actuator saturation observer continuously monitors the distance between the actuators torque vector and the maximum admissible torques vector in the n-dimensional space where n is the number of DoFs of the RHI. Informed by this, the actuator saturation controller ensures that, where possible, a minimum distance between the above two vectors is maintained. This is achieved by changing the secondary objective continuously from the ideal behaviour for the free-space motion to that for the hard contact case.

This keeps the control effort continuous and avoids disruptions to the performance that would result in the absence of a continuous change between the two secondary objectives. This research is the basis for a framework that can be used to design a haptic robot with a large workspace, relatively small apparent inertia, superior manipulability, and large enough force feedback.

This paper makes it possible for a user to exercise better (i.e., more efficient/precise and with higher fidelity) control and navigation of virtual or physical tools being manipulated from haptic interfaces by seamlessly integrating automatic control and task-dependent performance-related cost function optimization. For specific applications in surgery, this is part of a bigger tendency to only delegate the computationally-expensive aspects of robot-assisted intervention to the machine and keep the human operator (i.e., the clinician) in the loop and in charge of completing the main purpose of the intervention [33].

This paper is organized in sections as follows. Section II gives preliminaries while a null-space task-dependent controller is developed in Section III. In Section IV, experimental results are reported to verify the practicality of the proposed control strategy. Concluding remarks appear in Section V.

II. Preliminaries

Consider a redundant haptic interface with its end effector in an m-dimensional Cartesian space, X, and with an n-dimensional vector of joint variables, q. The joints' velocity are transformed to the end effector's velocity through the Jacobian matrix, $J \in \mathbb{R}^{m\times n}$, as

$$\dot{x} = J\dot{q}. \tag{1}$$

For an RHI, joint-level control law can be calculated by leveraging the kinematic redundancy of the RHI through the null-space control as [34]

$$\tau = \tau_m + \tau_N, \tag{2}$$

where τ_N is the null-space controller defined as

$$\tau_N = (I - J^T J^{\#^T})\tau_S. \tag{3}$$

τ_S is an $n \times 1$ torque vector corresponding to the secondary task in the joint space and does not create any end effector force/torque, I is the $n \times n$ identity matrix, and $J^{\#}$ is the generalized inverse of the Jacobian matrix defined as [35]

$$J^{\#} = M_q^{-1} J^T [J M_q^{-1} J^T]^{-1}, \tag{4}$$

in which $M_q \in \mathbb{R}^{n\times n}$ is the joint-space inertia matrix. In equation (2), τ_m is the corresponding $n \times 1$ joint control law to a given $m \times 1$ Cartesian space primary task control law, F_m, related by

$$\tau_m = J^T F_m. \tag{5}$$

III. Joint Space Secondary Objective

A secondary objective can be achieved by using a null-space controller, which works in parallel with the controller for the primary task. The null-space controller projects a suitable vector in the null-space of the RHI's Jacobian matrix. In the gradient projection approach [9], which is utilized here, this vector is selected as the gradient of a desired cost function $\nu(q)$. Conflicts between the primary-task controller and secondary objectives are handled in an assigned order of priority, i.e., a lower-priority objective is satisfied only in the null space of a higher-priority objective. The null-space control law, τ_S, which realizes a secondary objective is calculated as

$$\tau_S = -\beta \frac{\partial \nu(q)}{\partial q} - K_d \dot{q}, \tag{6}$$

where β is a suitable scalar step size and K_d is a damping scalar. With this choice of τ_N, the robot tries to decrease the value of the cost function, $\nu(q)$, while executing a primary time-varying task.

A. Cost Function Selection

The secondary objective selection is application-driven, i.e., the specific application regulates the requirements of the secondary objective. Manipulability ellipsoid (ME) of a robot, which was first introduced by Yoshikawa [36], indicates the ability to perform motion and exert force along with the different task directions in a given joint configuration. Thus, a secondary objective based on the manipulability ellipsoid can be utilized to resolve the configuration of the RHI for a desired task performance. For this, a desired ME can be defined based on the requirements and direction of the task, and then the configuration of the RHI is altered such that its ME matches the desired one. The Cartesian space force manipulability ellipsoid (FME) for an RHI is defined as $\mathcal{M} = (JJ^T)^{-1}$ because it maps a hyper-sphere in the joint space to an ellipsoid in the Cartesian space:

$$\|\tau\|^2 = \tau^T\tau = \Gamma^T(JJ^T)\Gamma = \Gamma^T\mathcal{M}^{-1}\Gamma \leq 1. \tag{7}$$

Here, τ is the joint torque vector, and Γ is an m-dimensional output force/torque vector. It is essential to note that the FME is the inverse of the velocity ME (VME), JJ^T. This means that the direction along which the RHI has the largest force/torque feedback capability is perpendicular to the direction along which the user can move the end-effector of the RHI with minimum joints movement to evoke minimum joint friction and thus distortion to the user's perception.

To be more clear, let us define the reflected joint friction ellipsoid at the end-effector as

$$\|F_q\|^2 = F_q^T F_q = F_x(JJ^T)F_x \leq 1 \tag{8}$$

where F_q is the vector of the joint friction torques and F_x is the vector of friction forces/torques reflected at the end-effector. By comparing (7) and (8), it can be seen that along the direction that the robot has the maximum force capability, the reflected joint friction at the end-effector is also maximum.

In (7), the RHI's actuators torque limits are not explicitly taken into account. During interactions between a user and an RHI, it is likely to require large torques in response to an unexpected situation; e.g., contacting with a solid object. Therefore, a more accurate FME can be calculated by scaling the joints torque with $W = \text{diag}(\frac{1}{\mathcal{T}_i})$, where $\mathcal{T}_i$ is the torque

limit for the ith joint, i.e., $|\tau_i| \leq \mathcal{T}_i$ [37]. Now, the modified FME is calculated as

$$\hat{\mathcal{M}} = (JWWJ^T)^{-1}. \tag{9}$$

The user operates the RHI in two cases, namely, free-space motion and in contact with the environment. For both cases, the user should not feel any distorted perception as the result of the RHI's joints friction. This defines the requirement of low back-drive friction for the RHI. Also, when there is a contact with the environment, the RHI should be able to provide adequate force feedback and stiffness such that the user feels the true large stiffness of an environment. This means that the joints' actuator of the RHI should not be saturated while rendering a stiff environment for the user. Therefore, two situations can be defined for the RHI; the first situation is when the RHI's actuators are far away from saturation, whereas the second situation is when the RHI's actuators are near their saturation levels. For each of these situations, a desired FME needs to be defined to meet the requirements of the task.

In [17], it is shown that by aligning the minor axis of the FME (major axis of VME) of an RHI along the desired direction of motion, the interference of joints friction of the RHI with the user's perception of the environment stiffness is minimized. In another work, the major axis of the FME of a redundant robot is aligned with the desired direction to maximize the force output capability of the robot by avoiding joints actuator saturation [38]. Therefore, for the first situation in which the RHI's actuators are far from their saturation levels (i.e., free-space movement and soft-tissue contact), we propose to design the desired FME such that its minor axis is aligned with the direction of the movement or contact to minimize the effect of joints friction. For the second situation (hard contacts), the major axis of the proposed desired FME is aligned with the direction of the contact to maximize the force feedback capability of the RHI. To illustrate this, let us consider a planar task in which the user moves the end effector of the RHI along a straight path in free-space and hits a rigid virtual wall at the end of the path. Assume that rendering the rigid virtual wall would put the RHI's actuators near their saturation levels. The desired FMEs are depicted in Fig. 2. Although in theory an ideal desired FME is a line, such an FME will take the RHI to a singular configuration, which is undesirable. Therefore, the minor axis of the FME should be designed small but not zero.

Here, we employ a geometry-aware cost function for the secondary objective to match the FME of the RHI to the desired FME. The cost function, ν, is defined as

$$\nu = \text{logdet}(\frac{\hat{\mathcal{M}} + \mathcal{M}^{des}}{2}) - \frac{1}{2}\text{logdet}(\hat{\mathcal{M}}\mathcal{M}^{des}) \tag{10}$$

in which $\mathcal{M}^{des}$ is the desired FME. The force manipulability ellipsoid is a symmetric positive definite matrix. Introduced by Cherian *et al.* [39], (10) forms a distance function for symmetric positive definite matrices that is convex. It has been shown that this function and its derivative are computationally less expensive than classical Riemannian distance functions. Also, Rozo *et al.* [40] have employed this distance function for matching the velocity manipulability of a redundant robot to a

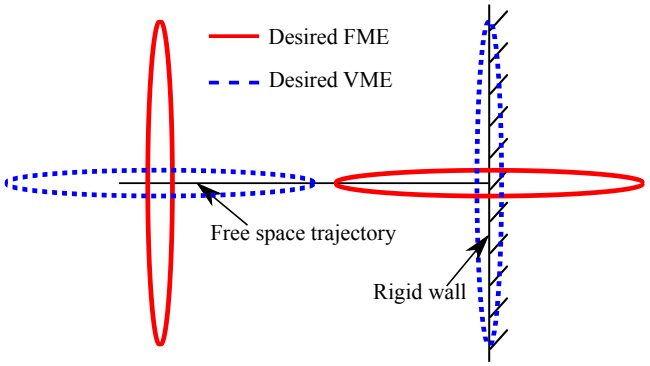

Fig. 2. Desired FME and VME for a planar task. The principal axes of the FME coincide with that of the VME with the inverse dimension of length.

desired one. They have also shown that the convergence rate of this distance function is much faster than the maximization of the major-axis alignment method used in [38]. Thus, (10) has been employed in this work to match the FME of the RHI to the desired one based on the requirements of a given task.

Using the symmetric positive definiteness property of the desired manipulability ellipsoid, it can be calculated as $\mathcal{M}^{des} = \mathcal{J}\mathcal{J}^T$, where $\mathcal{J}$ is an $m \times n$ matrix. Matrix $\mathcal{J}$ can be decomposed using singular value decomposition as $\mathcal{J} = U\Sigma\Omega^T$, where U is an unitary $m \times m$ matrix, Σ is a diagonal $m \times n$ matrix and Ω is an unitary $n \times n$ matrix. Thus, the desired FME can be written as

$$\mathcal{M}^{des} = U\Sigma\Omega^T\Omega\Sigma^T U^T = U\Sigma\Sigma^T U^T = U\Lambda U^T. \tag{11}$$

Here, U can be regarded as the rotation matrix, which indicates the direction of the principal axes of the FME, and the diagonal elements of the Λ matrix determine the length of the principal axes. More details on the selection of U and Λ matrices are given below.

First, let us consider a situation in which the RHI's actuators are far away from saturation levels. As stated before, to reduce the reflected joints friction at the end-effector of the RHI and consequently minimize the distortion caused by RHI on the user's perception of the environment, the minor axis of the FME needs to be aligned along the direction of motion. If $u_F \in \mathbb{R}^m$ is the unit vector corresponding to the direction of motion, the desired FME for this situation is defined as

$$\mathcal{M}^{des}_{Free} = U_F \underbrace{\begin{bmatrix} \begin{bmatrix} \zeta \\ 0_{(m-1)\times 1} \end{bmatrix}_{m\times 1}, & \begin{bmatrix} 0_{1\times(m-1)} \\ \mathcal{K}I_{(m-1)} \end{bmatrix}_{m\times(m-1)} \end{bmatrix}}_{\Lambda_{Free}} U_F^T \tag{12}$$

where U_F is calculated from singular value decomposition (SVD) of u_F as $u_F = U_F\Sigma_F V_F^T$. Parameters ζ and $\mathcal{K}$ are the constant scalar scaling factors that determine the length of the minor axis and the major axes of the desired FME, respectively. It appears that $\mathcal{K}$ should be equal to infinity and ζ should be equal to zero for best results. However, with these values, the RHI would be put into a singular configuration, which is undesirables. Therefore, $\mathcal{K}$ and ζ are proposed as $\mu\lambda_{max}\{\hat{\mathcal{M}}_0\}$ and $\frac{1}{\mu}\lambda_{min}\{\hat{\mathcal{M}}_0\}$, respectively. Here, $\lambda_{max}\{\hat{\mathcal{M}}_0\}$ is the maximum eigenvalue and $\lambda_{min}\{\hat{\mathcal{M}}_0\}$

is the minimum eigenvalue of the FME of the RHI at the non-singular home configuration. The home configuration is created by a particular set of joint positions of the RHI where the robot goes to when it is powered on. Therefore, ζ and $\mathcal{K}$ are unique and constant for each RHI. Also, μ is an appropriately selected scaling factor to shape the desired FME. It should be noted that ζ and $\mathcal{K}$ parameters are constant, and these two parameters are set prior to the experiments to shape the desired FME. In our experience, this selection of $\mathcal{K}$ and ζ assures that the null space controller puts the configuration of the RHI far away from the singularity while achieving the desired performance.

Now, consider the situation in which the RHI's actuators are near their saturation levels and the environment force, F_e, is presented to the user through the RHI. For this situation, the desired FME is calculated as

$$\mathcal{M}^{des}_{Stiff} = U_e \underbrace{\left[\begin{bmatrix} \mathcal{K} \\ 0_{(m-1)\times 1} \end{bmatrix}_{m\times 1}, \quad \begin{bmatrix} 0_{1\times(m-1)} \\ \zeta I_{(m-1)} \end{bmatrix}_{m\times(m-1)}\right]}_{\Lambda_{Stiff}} U_e^T. \tag{13}$$

This ellipsoid is spanned using the SVD of the environment force vector as $F_e = U_e \Sigma_e V_e^T$. By using (13), the major axis of $\mathcal{M}^{des}_{Stiff}$ is aligned with direction of the environment force.

1) Example: To elaborate the concept, consider a 3 DoF planar RHI with the links length $L_i = [0.25,\ 0.25,\ 0.25]$ m, $i = 1, 2, 3$. The link masses are equal to 0.5 Kg for all links and assumed to be located at the center of mass of each link, i.e., the middle point of each link. The joint torques bounds are given as $|\mathcal{T}_i| \leq 0.5$ N.m, and thus the FME scaling matrix is calculated as $W = \text{diag}\{2,\ 2,\ 2\}$. At the initial configuration of $q_i = [\frac{\pi}{6},\ -\frac{\pi}{3},\ -\frac{3\pi}{4}]$ rad, the RHI is supposed to provide force feedback to the user when he/she holds the end-effector of the RHI fixed in the task space. The desired force is $F_e = [3.5\sin(t\pi/2),\ 0]^T$ N, where t is time. Thus, the joint space control law corresponding to this desired force is $\tau_m = J^T F_e$. For this example, the FME of the 3-DoF RHI is matched with the desired FMEs using the cost function (10). Fig. 3 shows the torques of the RHI joints and the output force feedback of the RHI at three different configurations: the initial configuration, the optimized configuration matching the FME of the RHI to $\mathcal{M}^{des}_{Free} = \text{diag}\{.2 \times 2.6,\ 5 \times 5.8\}$, and the optimized configuration matching the RHI's FME to $\mathcal{M}^{des}_{Stiff} = \text{diag}\{5 \times 5.8,\ .2 \times 2.6\}$, (assuming $\mu = 5$).

To preserve the force feedback direction for the above simulation studies, a scaling factor α is implemented to scale the desired force feedback as soon as one of the RHI's actuators is saturated. By matching the RHI's FME with $\mathcal{M}^{des}_{Free}$, the force feedback capability of the RHI is decreased in return for better manipulability in the desired direction for the free-space movement and soft-tissue manipulation. On the other hand, when the FME of the RHI is matched with $\mathcal{M}^{des}_{Stiff}$, the force feedback capability of the RHI is enhanced and the desired force feedback is rendered without any saturation for the joint's actuators. Fig. 4 illustrates the initial configuration of the RHI, the optimized configurations of the RHI for the free motion and soft contact (matching its FME to $\mathcal{M}^{des}_{Free}$) and its optimized configuration for the hard contacts (matching its FME to$\mathcal{M}^{des}_{Stiff}$), and the FMEs.

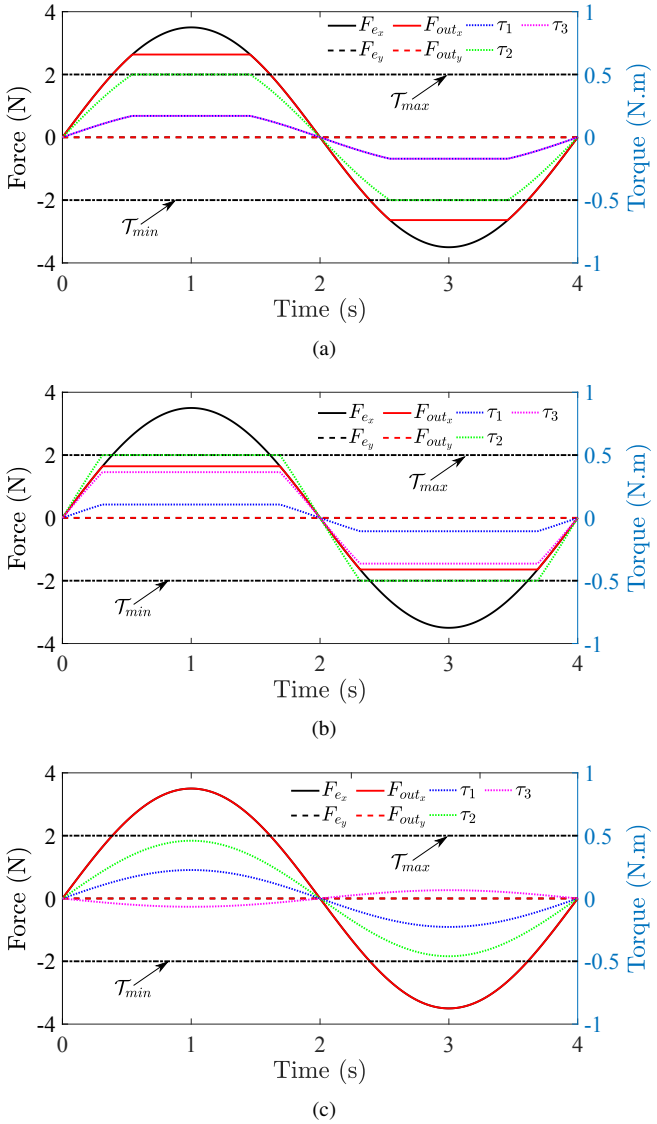

Fig. 3. Joint torques and output force feedback of a 3-DoF RHI at (a) initial configuration, (b) optimized configuration by matching its FME to $\mathcal{M}^{des}_{Free}$, and (c) optimized configuration by matching its FME to $\mathcal{M}^{des}_{Stiff}$.

B. Actuator Saturation Controller

As can be seen in Fig. 2, the desired FME remains constant in the free-space motion and soft-tissue manipulation, and the minor axis of the FME is aligned with the trajectory, but for the case of stiff contact the desired FME is transformed in such a way that the major axis of the FME is aligned with the contact direction. Therefore, a smooth transition between the desired FMEs is required; otherwise, fast reconfiguration of the internal motion of RHI would happen which may cause RHI's internal motion instability, RHI self-collision, and/ or RHI collision with the user.

Here, the actuator saturation observer (ASO) is proposed to monitor the distance of the RHI's joint actuators torque from their saturation levels. Inspired by the work in [41], the ASO can be considered as the volume of a tank of actuators'

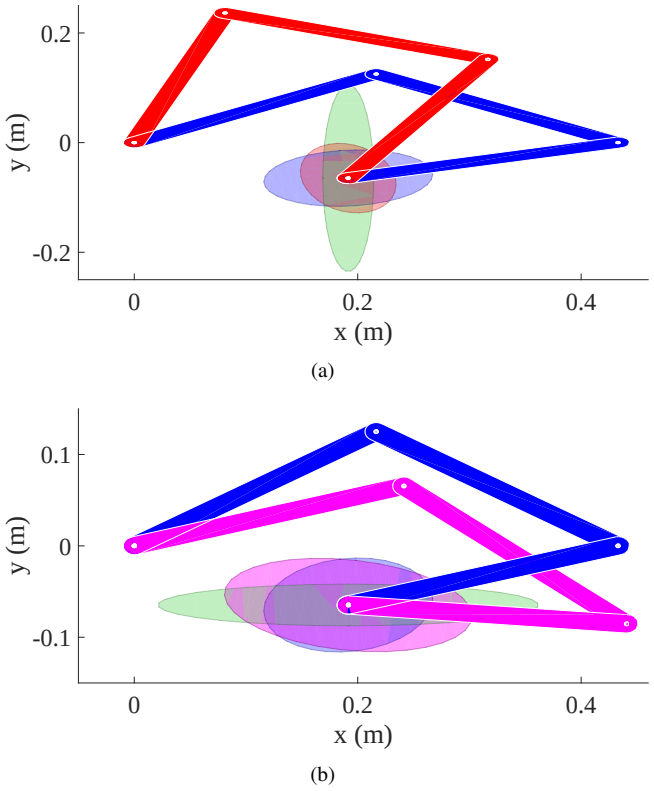

Fig. 4. RHI's initial configuration and initial FME in blue, the desired FMEs in green, (a) RHI's optimized configuration and FME for free-space movement and soft contact in red, and (b) RHI's optimized configuration and FME for hard contact in magenta. The FMEs are scaled for better visualization.

unused torque output capacity. When a task demands large actuator torques, this tank is used and can become empty over time. The volume of the tank is zero when one or more of the robot's actuators are saturated; even when only one actuator is saturated, the RHI loses the ability to apply *arbitrary* force vectors at its end-effector. The ASO informs the actuator saturation controller (ASC) to switch between the desired FMEs (i.e., from the desired free-space FME to the desired stiff-contact FME) to keep the actuators away from their saturation limits. The volume of the tank is defined as

$$V = \frac{1 - \exp(-S(-1)^n \prod_{i=1}^{n} \frac{(\tau_{m,i} - \mathcal{T}_{max,i})(\tau_{m,i} - \mathcal{T}_{min,i})}{(\mathcal{T}_{max,i} - \mathcal{T}_{min,i})^2})}{1 - \exp(-\frac{S}{4^n})}, \tag{14}$$

where n denotes the number of joints of the RHI, S is the scaling factor that determines the shape and thus the gradient of the ASO, and V is a scalar that spans the $[0, 1]$ interval. The ASO for a two-DoF robot, that has joint torques bounds $|\mathcal{T}_1| \leq 0.5$ N.m and $|\mathcal{T}_2| \leq 2$ N.m is depicted in Fig. 6. The ASO can be used for both redundant and non-redundant robots to determine how far the robot's actuators are from their saturation levels.

Now, the ASC selects the desired FME for the secondary objective based on the ASO as

$$\hat{\mathcal{M}}^{des} = \begin{cases} M^{des}_{Free}, & \text{if } V \geq \epsilon \\ M^{des}_{Stiff}, & \text{if } V < \epsilon \end{cases} \tag{15}$$

where ϵ is a threshold that determines how far from the saturation of RHI's actuator the transition happens between the FMEs.

Let us now look at the case where the transition between the desired FMEs is required. The transition among the desired FMEs occurs when there is a change in the primary task in the Cartesian space. As highlighted in Fig. 2, the transition for the FME happens when one or more of the RHI's joints actuator come close to their saturation levels. To ensure continuity with respect to time for the transition from a desired FME to another one, a continuous activation parameter Ω with the value between zero and one is required [42], [43]. Here, the desired FME for (10) is proposed to be calculated as the composition of two FMEs as

$$\mathcal{M}^{des} = \Omega M^{des}_{Free} + (1 - \Omega) M^{des}_{Stiff}. \tag{16}$$

Two instances need to be considered; the time of transition from M^{des}_{Free} to M^{des}_{Stiff} and vice versa. For the first case, the activation parameter is defined as

$$\Omega = \begin{cases} 1, & \text{if } V \geq \epsilon_1 \\ 0.5(1 + \cos(\pi \frac{t - t_0}{t_f - t_0})), & \text{if } V < \epsilon_1 \text{ and } t < t_f \\ 0, & \text{if } t \geq t_f \end{cases} \tag{17}$$

and for the second case, Ω is defined as

$$\Omega = \begin{cases} 0, & \text{if } V < \epsilon_2 \\ 0.5(1 - \cos(\pi \frac{t - t_0}{t_f - t_0})), & \text{if } V \geq \epsilon_2 \text{ and } t < t_f \\ 1, & \text{if } t \geq t_f \end{cases} \tag{18}$$

Here, t_0 and t_f represent the start and end time of the transition, respectively. ϵ_1 and ϵ_2 are appropriately designed thresholds. If only one ϵ is defined as a threshold for the transition between the FMEs, chattering can happen. In other words, slightly falling short of ϵ will cause a switch from $\mathcal{M}^{des}_{Free}$ to $\mathcal{M}^{des}_{Stiff}$ and slightly exceeding ϵ will cause a switch from $\mathcal{M}^{des}_{Stiff}$ to $\mathcal{M}^{des}_{Free}$. To avoid this, two separate thresholds (ϵ_1 and ϵ_2) are defined. The activation parameter and the transition between two FMEs are depicted in Fig. 7. The transition end time, t_f, defines how fast the transition is performed and it is obtained as a function of distance between the desired FMEs:

$$t_f = \rho \left\| M^{des}_{Free} - M^{des}_{Stiff} \right\|_F + t_0, \tag{19}$$

in which ρ is a suitable scaling factor and $\|.\|_F$ is the Frobenius norm. A block diagram of the control system is depicted in Fig. 5.

IV. Experimental Evaluation

In this section, experiments are performed to evaluate the proposed null space controller using a 4-DoF planar RHI. This RHI is made by coupling two 2-DoF HIs; a 2-DOF planar upper-limb rehabilitation robot (Quanser Inc., Markham, ON, Canada) and a 2-DoF PHANToM 1.5A (3D Systems Inc., Morrisville, NC, USA). Also, a force/torque sensor (50M31A3-I25, JR3 Inc., Woodland, CA, USA) is attached to the end-effector of the RHI to measure forces that are feedback to the user. MATLAB/Simulink (MathWorks Inc., Natick, MA,

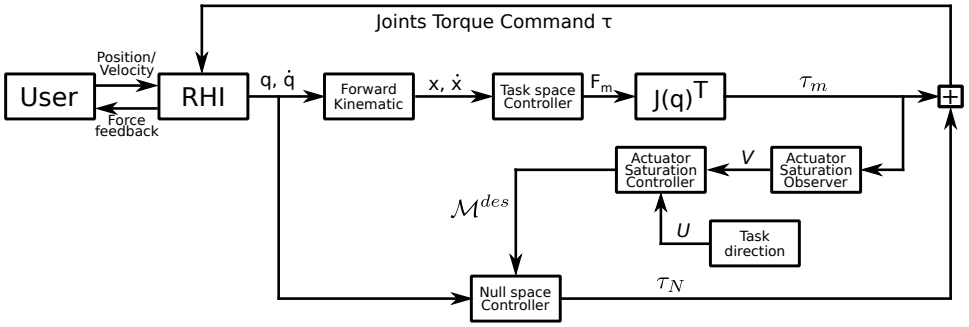

Fig. 5. Block diagram of the control system.

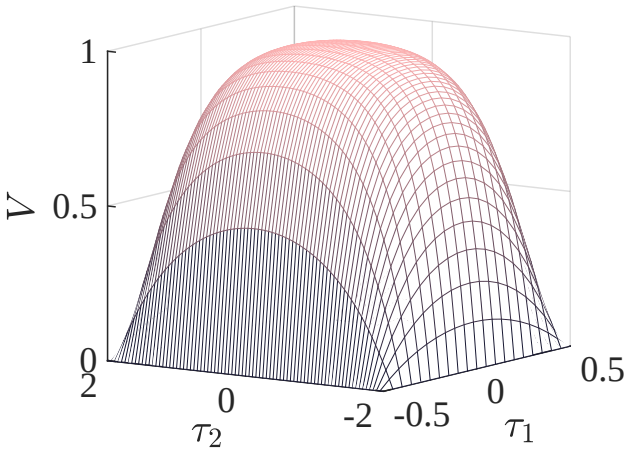

Fig. 6. The ASO for a two-DoF robot with $s = 50$.

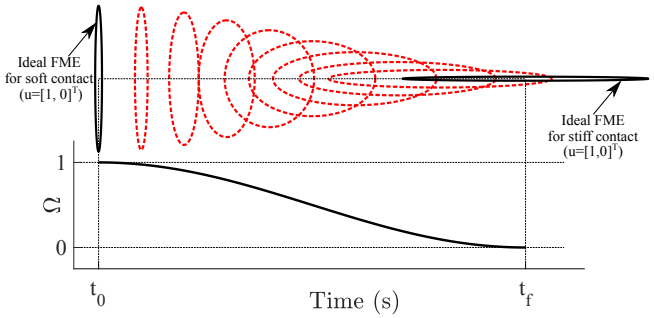

Fig. 7. (top) Transition between two FMEs which are shown in black ellipsoids and (bottom) Activation parameter Ω.

USA) with Quarc real-time control software (Quanser Inc., Markham, ON, Canada) is used to interface the RHI and the force sensor with the computer. Fig. 8 shows the experimental setup.

For the purpose of this experiment, the RHI has joint torques limitation programmed as $\mathcal{T}_i = [3,\ 3,\ 1,\ 1]$ N.m. The Jacobian matrix of the RHI is

$$J_{RHI} = \begin{bmatrix} -d_1 sq_1, & d_2 cq_2 - d_3 sq_{23} + d_4 cq_{24}, & -d_3 sq_{23}, & d_4 cq_{24} \\ d_1 cq_1, & d_2 sq_2 + d_3 cq_{23} + d_4 sq_{24}, & d_3 cq_{23}, & d_4 sq_{24} \end{bmatrix} \quad (20)$$

where s and c denote $sin(.)$ and $cos(.)$, respectively. $q_{ij} = q_i + q_j$ and $d_i = [0.254,\ 0.141,\ 0.21,\ 0.181]$ m, $i = 1, 2, 3, 4$, denotes the RHI's links length. Also, parameters μ, β, and K_d are selected equal to 5, 20, and 0.1, respectively. The home configuration of the RHI is defined as $q_i = [0,\ 0,\ 0,\ 0]$. Thus, $\mathcal{K}$ and ζ are calculated as 123 and 3.3, respectively.

In the experiments, a user holds the end effector of the RHI and palpates a virtual environment along the right-hand direction (i.e., $u = [0,\ 1]^T$) through it. The virtual environment is modelled as a spring with constant stiffness. In the experiments, the user palpates the virtual environment starting from a fixed point in the workspace of the RHI. The starting point is given as $X_0 = [0.5,\ 0.1]^T$ m. The Cartesian space control law used in the experiments is

$$F_m = K_e \delta X \quad (21)$$

where K_e is the stiffness of the virtual environment and δX is the position deviation from the starting point. The virtual environment is modelled as $K_e = 1000$ N/m to create a stiff environment.

To show the effectiveness of the proposed methods, the experiments are carried out in two scenarios. The objective of the first scenario is to show the enhanced force feedback capability of the RHI by using the proposed null-space controller and matching the FME of the RHI with the desired FME. As stated before, a single desired FME for the secondary objective cannot be used due to the conflicting requirements of having large force feedback capability for the hard contact case and having large velocity manipulability for the free motion and soft contact case. Therefore, in the second scenario, the proposed transition method between the desired FMEs is evaluated.

Two cases are considered for the first scenario. (A) The palpation is performed on the environment through the RHI with matching the FME of the RHI with the desired FME, $\hat{\mathcal{M}}^{des}$, with $\epsilon = 0$, i.e., the desired FME is $\mathcal{M}^{des}_{Free}$. (B) The palpation is performed with FME matching with $\epsilon = 1$, i.e., the desired FME is $\mathcal{M}^{des}_{Stiff}$. In (A), the force feedback scaling is performed when one or more joints actuator of the RHI are saturated to preserve the direction of the force feedback, and the minor axis of the desired FME is aligned with the direction of motion (contact). For this case, the desired FME is $\hat{\mathcal{M}}^{des} = \mathcal{M}^{des}_{Free} = \text{diag}\{123,\ 3.3\}$. In (B), the major axis of the desired FME is always aligned with the direction of motion (contact), and it is calculated using (13) as $\hat{\mathcal{M}}^{des} = \mathcal{M}^{des}_{Stiff} = \text{diag}\{3.3,\ 123\}$.

Fig. 9 shows the experimental results for the first scenario. In this figure, the measured force using the force/torque sensor,

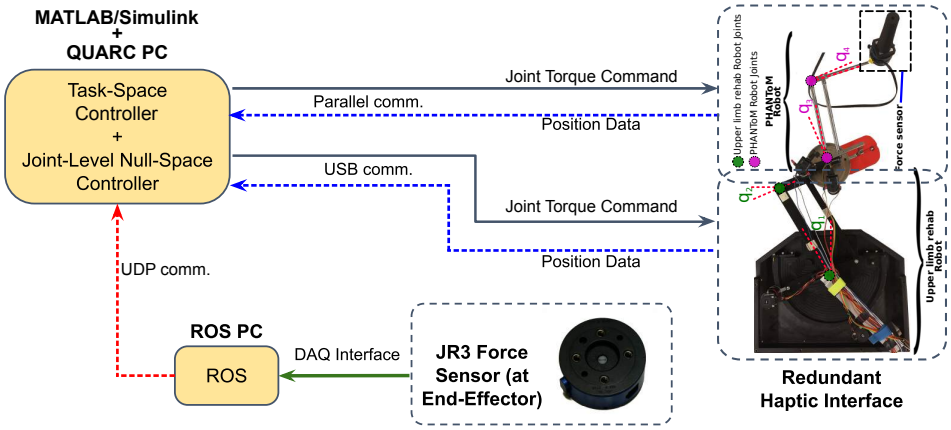

Fig. 8. Experimental setup.

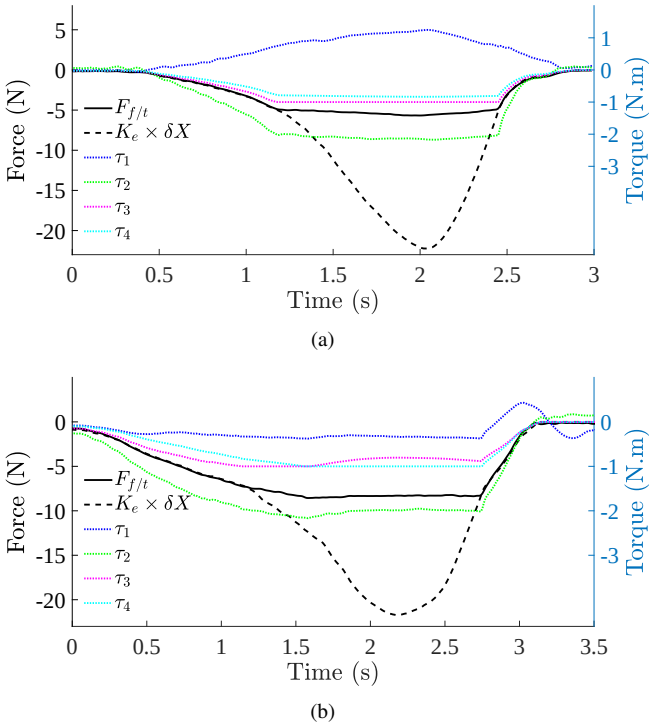

(a)

(b)

Fig. 9. Experimental results at the optimized configuration by matching the RHI's FME to (a) $\mathcal{M}_F^{des}$ and (b) $\mathcal{M}_C^{des}$.

the desired force ($K_e \times \delta X$), and the torque of the actuators are illustrated. As it can be seen in this figure, the maximum force feedback of the RHI in case (B) (Fig. 9(b)) is 51% more than the force feedback capability of the RHI in case (A) (Fig. 9(a)). As a result, the user feels the environment more stiff in case (B). This shows that the force feedback capability of the RHI is enhanced by leveraging the kinematic redundancy before the occurrence of joints' actuator saturation.

Thus far, it is shown that the force feedback capability of the RHI when its FME is matched with $\mathcal{M}_{Stiff}^{des}$ using the null-space controller is larger than that of the RHI when its FME is matched with $\mathcal{M}_{Free}^{des}$. Here, system identification experiments are performed to show that the back-drive friction and the Cartesian-space inertia of the RHI in case (A) are lower that

TABLE I

EXPERIMENTAL VALUES FOR INERTIA M_x, FRICTION PARAMETER Φ, AND MAXIMUM FORCE FEEDBACK CAPABILITY OF THE PLANAR 4-DOF RHI ALONG $u = [0,\ 1]^T$ FOR THE END-EFFECTOR POSITION $[0.5,\ 0.1]$ M.

Desired FME	M_x (Kg)	Φ (N.s/m)	F_{max} (N)
$\mathcal{M}_{Free}^{des}$	0.036	0.2953	-5.674
$\mathcal{M}_{Stiff}^{des}$	0.125	0.6325	-8.564

of the RHI in case (B). To identify the back-drive friction and the Cartesian-space inertia of the RHI, its end-effector dynamics is modelled for simplicity as

$$M_x \ddot{X} + F_f = F_{ext}, \tag{22}$$

where M_x is the Cartesian-space inertia, F_f is the back-drive friction force, F_{ext} is the external force applied to the end-effector of the RHI, and X is the position of the end-effector. X, M_x, F_f, and F_{ext} are scalars as the experiments are performed along one axis (i.e., along $u = [0,\ 1]^T$). Also, the back-drive friction is modelled as the viscose friction $F_f = \Phi \dot{X}$, where Φ is the friction parameter.

System identification experiments are carried out for two cases: the configuration of the RHI being determined by matching its FME with $\mathcal{M}_{Stiff}^{des}$ and with $\mathcal{M}_{Free}^{des}$. Ten trials are conducted for each case to identify M_x and Φ. In each trial, first, the end-effector of the RHI is placed at $[0.5,\ 0.05]^T$ m. Next, a constant external force in the range of $0.5 - 1.5$ N is applied to the end-effector of the RHI, and the position along $u = [0,\ 1]^T$, velocity, and acceleration of the end-effector are measured at $[0.5,\ 0.1]^T$ m point. The end-effector is placed 5 cm away from the point of interest to eliminate the effects of Coulomb friction in the experiments. The measured signals are filtered using a zero-phase 5^{th}-order Butterworth lowpass filter. Then, M_x and Φ are identified by applying the linear least-squares regression to (22). The experimental results for the Cartesian-space inertia and the back-drive friction, as well as the maximum force feedback capability, are listed in Table I.

Table I shows that for the same end-effector position of RHI, the inertia, back-drive friction, and force feedback capability are lower for the configuration being determined by the desired

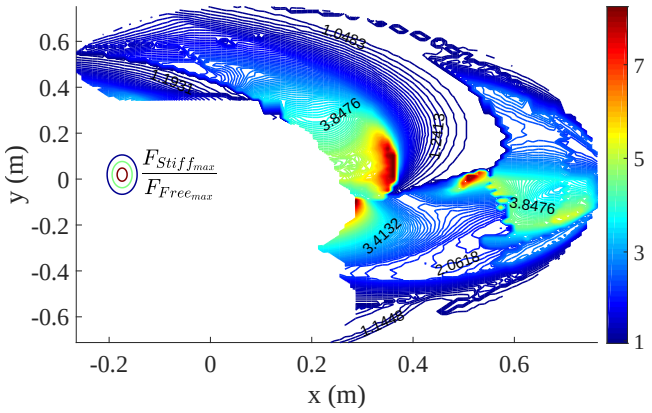

Fig. 10. The ratio of maximum force feedback capability of the four-DoF RHI with the configuration being determined by matching its FME to $\mathcal{M}_F^{des}$ and $\mathcal{M}_C^{des}$ over the entire workspace.

FME for the free space $\mathcal{M}_{Free}^{des}$. Having low inertia and back-drive friction is desirable for the free-space movement and soft contact, which leads to the smaller sensation of RHI's linkage and joint friction. However, large force feedback capability is required to recreate a stiff environment for the user. Therefore, for the stiff environment, the desired FME should be set as $\mathcal{M}_{Stiff}^{des}$ to achieve larger force feedback capability at the price of larger inertia and friction.

As the experiment for this scenario was conducted for a given starting point at the workspace, a simulational study was performed to show the force feedback enhancement across the entire workspace. The same four-DoF RHI that was used in the experiment is employed in the simulational study. For each point of the RHI's workspace, the maximum force feedback capability along $u = [0,\ 1]^T$ is calculated for two cases: Case (I) the manipulability of the RHI is matched with $\mathcal{M}_{Free}^{des} = \text{diag}\{123,\ 3.3\}$ (minimize the effect of joints friction at the end-effector), and Case (II) the manipulability of the RHI is matched with $\mathcal{M}_{Stiff}^{des} = \text{diag}\{3.3,\ 123\}$ (maximize the force feedback capability of the robot). The simulational results are shown in Fig. 10. As the result of the study shows, over the entire workspace, the force feedback capability of the RHI with the joints configuration being determined by matching its FME with $\mathcal{M}_{Stiff}^{des}$ is considerably larger than the force feedback capability of the RHI with its joints configuration being determined by matching its FME with $\mathcal{M}_{Free}^{des}$ at the same end-effector location.

In the second scenario, the performance of the proposed transition method between the secondary objectives in terms of preventing the discontinuity in null-space control effort is evaluated. The palpation task is performed (C) with and (C') without the proposed transition method. The parameter ϵ_1 that determines when the transition from $\mathcal{M}_{Free}^{des} = \text{diag}\{123,\ 3.3\}$ to $\mathcal{M}_{Stiff}^{des} = \text{diag}\{3.3,\ 123\}$ occurs is selected equal to 0.7 and the parameter ϵ_2 that regulate the switching from $\mathcal{M}_{Stiff}^{des}$ to $\mathcal{M}_{Free}^{des}$ is selected equal to 0.95. For the (C) case, the desired FME is calculated form (15) and for the (C') case, the desired FME is calculated using (16). Parameter ρ is selected equal to 0.003 so that the transition performed in 0.5 second.

In Figs. 11(a) and 11(b) the comparison between the behaviour of the RHI without and with the proposed transition method are shown, respectively. As it can be seen in Fig. 11(a), discontinuity in the control effort causes the interference of RHI's internal motion with the motion and force of the RHI's end-effector when the desired FME is switched suddenly from $\mathcal{M}_{Free}^{des}$ to $\mathcal{M}_{Stiff}^{des}$. However, by using the proposed method, the transition between the desired FMEs is carried out smoothly (see Fig. 11(b)). For the (C') case, the ASO and the activation parameter are illustrated in Fig. 11(c). As can be seen in this figure, the transition starts when the ASO (volume of the tank) becomes smaller than 0.7. The transition slows down the drainage of the tank, which keeps the actuators away from their saturation levels. Therefore, the RHI can provide large force feedback.

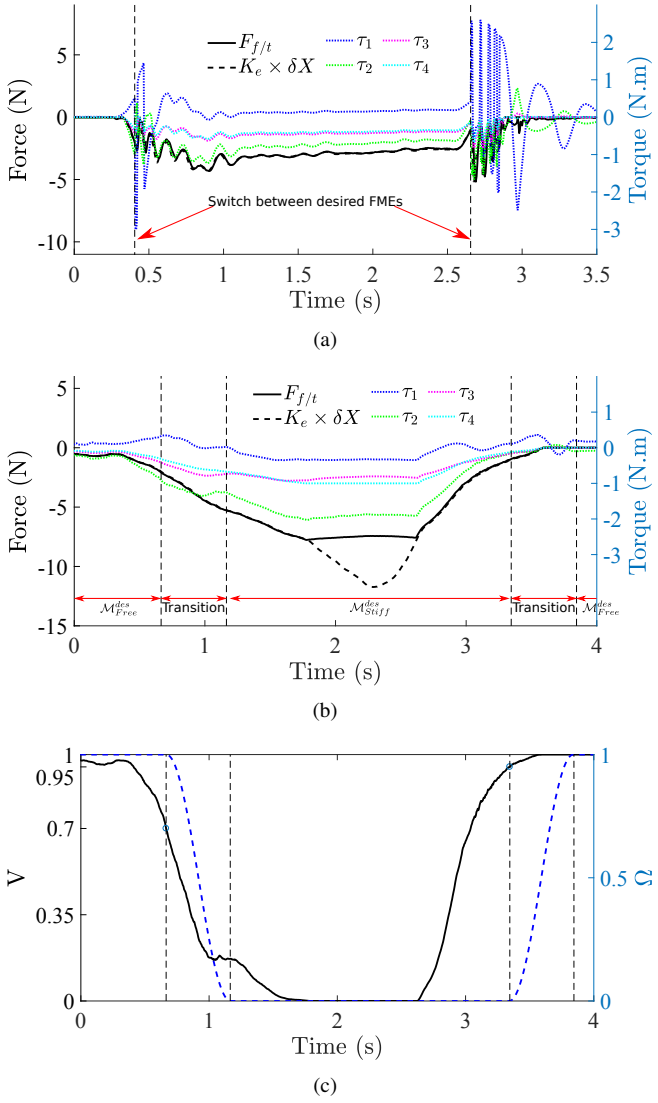

Fig. 11. Experimental results (a) without and (b) with the proposed transition method between the desired FMEs. (c) The ASO (volume of the tank) V in solid black line and activation parameter ω in dashed blue line when the transition method is utilized.

V. Concluding Remarks

In this paper, we proposed a null-space controller for redundant haptic interfaces. The objective was to enable a user

to experience believable interactions with an environment, be it free space, soft contact, or hard contact. The proposed null-space controller leverages the kinematic redundancy of the RHI toward secondary objectives to optimize the interaction of the user with the environment. Two secondary objectives based on the task requirements were proposed in this paper. Also, a transition method based on the actuator saturation observer was proposed to prevent discontinuity of the control effort when switching between the secondary objectives was required. The actuator saturation observer monitors the distance between the actuators torque and their saturation levels. When the RHI's actuators are far away from their saturation levels, an appropriate secondary objective is active and manipulates the internal motion of the RHI to increase its velocity manipulability, and consequently decrease the interference of the friction forces and kinematics of the RHI with the user-environment interaction. This secondary objective is replaced with another secondary objective when the RHI's actuators become close to their saturation levels, which can happen when rendering hard contacts. It was shown that the RHI's force feedback capability is configuration dependable, and by appropriately manipulating the internal motion of the RHI, it can be enhanced. The experiments showed 51% enhancement in the force feedback capability of the RHI using the proposed methods. Also, experiments showed the practicality of the proposed transition method by preventing the discontinuity in the control effort for the RHI.

REFERENCES

[1] M. Tavakoli, A. Aziminejad, R. Patel, and M. Moallem, "High-fidelity bilateral teleoperation systems and the effect of multimodal haptics," *IEEE Transactions on Systems, Man and Cybernetics – Part B*, vol. 37, no. 6, pp. 1512–1528, December 2007.

[2] A. Torabi, M. Khadem, K. Zareinia, G. R. Sutherland, and M. Tavakoli, "Manipulability of teleoperated surgical robots with application in design of master/slave manipulators," in *2018 International Symposium on Medical Robotics (ISMR)*, March 2018, pp. 1–6.

[3] T. H. Massie and J. K. Salisbury, "The phantom haptic interface: A device for probing virtual objects," in *Proceedings of the ASME Dynamic Systems and Control Division*, 1994, pp. 295–301.

[4] S. Grange, F. Conti, P. Rouiller, P. Helmer, and C. Baur, "Overview of the delta haptic device," in *EUROHAPTICS 2001*, 2001, pp. 164–166.

[5] L. J. Stocco, S. E. Salcudean, and F. Sassani, "Optimal kinematic design of a haptic pen," *IEEE/ASME Transactions on Mechatronics*, vol. 6, no. 3, pp. 210–220, 2001.

[6] J. E. Colgate and J. M. Brown, "Factors affecting the z-width of a haptic display," in *Proceedings of the 1994 IEEE International Conference on Robotics and Automation*, May 1994, pp. 3205–3210 vol.4.

[7] R. Ellis, O. Ismaeil, and M. Lipsett, "Design and evaluation of a high-performance haptic interface," *Robotica*, vol. 14, no. 03, p. 321, 1996.

[8] E. Samur, *Performance metrics for haptic interfaces*. Springer Science & Business Media, 2012.

[9] B. Siciliano, "Kinematic control of redundant robot manipulators: A tutorial," *Journal of Intelligent and Robotic Systems*, vol. 3, no. 3, pp. 201–212, 1990.

[10] I. Nisky, M. H. Hsieh, and A. M. Okamura, "Uncontrolled manifold analysis of arm joint angle variability during robotic teleoperation and freehand movement of surgeons and novices," *IEEE Transactions on Biomedical Engineering*, vol. 61, no. 12, pp. 2869–2881, dec 2014.

[11] S. Chiaverini, G. Oriolo, and A. A. Maciejewski, "Redundant robots," in *Springer Handbook of Robotics*, B. Siciliano and O. Khatib, Eds. Cham: Springer International Publishing, 2016, pp. 221–242.

[12] F. Ficuciello, L. Villani, and B. Siciliano, "Variable impedance control of redundant manipulators for intuitive human – robot physical interaction," *Transactions on Robotics*, vol. 31, no. 4, pp. 1–14, 2015.

[13] M. Ueberle, N. Mock, and M. Buss, "VISHARD10, a novel hyper-redundant haptic interface," in *Proceedings - 12th International Symposium on Haptic Interfaces for Virtual Environment and Teleoperator Systems, HAPTICS*, 2004, pp. 58–65.

[14] O. Baser, E. I. Konukseven, and T. Balkan, "Optimal posture control for a 7 dof haptic device based on power minimization," in *International Conference on Human Haptic Sensing and Touch Enabled Computer Applications*. Springer, 2008, pp. 555–560.

[15] Ö. BAŞER and E. I. Konukseven, "7-dof haptic device and interface design," *Turkish Journal of Electrical Engineering & Computer Sciences*, vol. 21, no. 2, pp. 493–499, 2013.

[16] J. K. Salisbury Jr, A. J. Madhani, G. S. Guthart, G. D. Niemeyer, and E. F. Duval, "Master having redundant degrees of freedom," 2004, uS Patent 6,684,129.

[17] A. Torabi, M. Khadem, K. Zareinia, G. R. Sutherland, and M. Tavakoli, "Application of a redundant haptic interface in enhancing soft-tissue stiffness discrimination," *IEEE Robotics and Automation Letters*, vol. 4, no. 2, pp. 1037–1044, April 2019.

[18] A. Barrow and W. Harwin, "Design and analysis of a haptic device design for large and fast movements," *Machines*, vol. 4, no. 1, pp. 1–19, 2016.

[19] H. S. Kim, "Kinematically redundant parallel haptic device with large workspace," *International Journal of Advanced Robotic Systems*, vol. 9, no. 6, p. 260, 2012.

[20] F. Gosselin, C. Andriot, F. Bergez, and X. Merlhiot, "Widening 6-dof haptic devices workspace with an additional degree of freedom," in *Second Joint EuroHaptics Conference and Symposium on Haptic Interfaces for Virtual Environment and Teleoperator Systems (WHC'07)*, March 2007, pp. 452–457.

[21] N. Nath, E. Tatlicioglu, and D. M. Dawson, "Teleoperation with kinematically redundant robot manipulators with sub-task objectives," *Robotica*, vol. 27, pp. 1027–1038, 2009.

[22] A. Zakerimanesh, F. Hashemzadeh, A. Torabi, and M. Tavakoli, "Controlled synchronization of nonlinear teleoperation in task-space with time-varying delays," *International Journal of Control, Automation and Systems*, vol. 0, no. 0, pp. 1–9, 2019.

[23] D.-Y. Hwang and B. Hannaford, "Teleoperation performance with a kinematically redundant slave robot," *The International Journal of Robotics Research*, vol. 17, no. 6, pp. 579–597, 1998.

[24] P. Lambert and J. L. Herder, "A 7-dof redundantly actuated parallel haptic device combining 6-dof manipulation and 1-dof grasping," *Mechanism and Machine Theory*, vol. 134, pp. 349 – 364, 2019.

[25] D. Constantinescu, I. Chau, S. P. DiMaio, L. Filipozzi, S. E. Salcudean, and F. Ghassemi, "Haptic rendering of planar rigid-body motion using a redundant parallel mechanism," in *Proceedings 2000 ICRA. Millennium Conference. IEEE International Conference on Robotics and Automation. Symposia Proceedings (Cat. No.00CH37065)*, vol. 3, April 2000, pp. 2440–2445 vol.3.

[26] P. Buttolo and B. Hannaford, "Advantages of actuation redundancy for the design of haptic displays," in *Proceedings ASME Fourth Annual Symposium on Haptic Interfaces for Virtual Environment and Teleoperator Systems.*

[27] C. Gosselin and L.-T. Schreiber, "Redundancy in Parallel Mechanisms: A Review," *Applied Mechanics Reviews*, vol. 70, no. 1, 01 2018, 010802.

[28] S. E. Salcudean and T. D. Vlaar, "On the emulation of stiff walls and static friction with a magnetically levitated input/output device," *Journal of Dynamic Systems, Measurement, and Control*, vol. 119, no. 1, pp. 127–132, 1997.

[29] N. Colonnese, A. F. Siu, C. M. Abbott, and A. M. Okamura, "Rendered and characterized closed-loop accuracy of impedance-type haptic displays," *IEEE Transactions on Haptics*, vol. 8, no. 4, pp. 434–446, Oct 2015.

[30] R. L'Orsa, C. J. Macnab, and M. Tavakoli, "Introduction to haptics for neurosurgeons," *Neurosurgery*, vol. 72, no. Supplement, pp. A139–A153, 2013.

[31] S. F. Atashzar, M. Shahbazi, M. Tavakoli, and R. V. Patel, "A grasp-based passivity signature for haptics-enabled human-robot interaction: Application to design of a new safety mechanism for robotic rehabilitation," *The International Journal of Robotics Research*, vol. 36, no. 5-7, pp. 778–799, 2017.

[32] M. Sharifi, H. Salarieh, S. Behzadipour, and M. Tavakoli, "Patient-robot-therapist collaboration using resistive impedance controlled tele-robotic systems subjected to time delays," *Journal of Mechanisms and Robotics*, vol. 10, no. 6, pp. 061 003–17, 2018.

[33] G.-Z. Yang *et al.*, "Medical robotics—regulatory, ethical, and legal considerations for increasing levels of autonomy," *Science Robotics*, vol. 2, no. 4, 2017.

[34] O. Khatib, "A unified approach for motion and force control of robot manipulators: The operational space formulation," *IEEE Journal on Robotics and Automation*, vol. 3, no. 1, pp. 43–53, February 1987.
[35] O. Khatib, "Inertial Properties in Robotic Manipulation: An Object Level Framework," *International Journal Of Robotics Research*, vol. 13, no. 1, pp. 19–36, 1995.
[36] T. Yoshikawa, "Manipulability of Robotic Mechanisms," *The International Journal of Robotics Research*, vol. 4, no. 2, pp. 3–9, 1985.
[37] P. Chiacchio, Y. Bouffard-Vercelli, and F. Pierrot, "Force polytope and force ellipsoid for redundant manipulators," *Journal of Robotic Systems*, vol. 14, no. 8, pp. 613–620, 1997.
[38] A. Ajoudani, N. G. Tsagarakis, and A. Bicchi, "Choosing poses for force and stiffness control," *IEEE Transactions on Robotics*, vol. 33, no. 6, pp. 1483–1490, Dec 2017.
[39] A. Cherian, S. Sra, A. Banerjee, and N. Papanikolopoulos, "Jensen-bregman logdet divergence with application to efficient similarity search for covariance matrices," *IEEE Transactions on Pattern Analysis and Machine Intelligence*, vol. 35, no. 9, pp. 2161–2174, Sep. 2013.
[40] L. Rozo, N. Jaquier, S. Calinon, and D. G. Caldwell, "Learning manipulability ellipsoids for task compatibility in robot manipulation," in *2017 IEEE/RSJ International Conference on Intelligent Robots and Systems (IROS)*, Sept 2017, pp. 3183–3189.
[41] A. Dietrich, X. Wu, K. Bussmann, C. Ott, A. Albu-Schäffer, and S. Stramigioli, "Passive hierarchical impedance control via energy tanks," *IEEE Robotics and Automation Letters*, vol. 2, no. 2, pp. 522–529, April 2017.
[42] J. Lee, N. Mansard, and J. Park, "Intermediate desired value approach for task transition of robots in kinematic control," *IEEE Transactions on Robotics*, vol. 28, no. 6, pp. 1260–1277, Dec 2012.
[43] S. Kim, S. Y. Lee, K. Jang, Y. Lee, S. Park, and J. Park, "Continuous Task Transition Approach for Robot Controller based on Hierarchical Quadratic Programming," *IEEE Robotics and Automation Letters*, vol. 4, no. 2, pp. 1603–1610, 2019.